Analytica Chimica Acta 1333 (2025) 343399

Contents lists available at ScienceDirect

Analytica Chimica Acta

journal homepage: www.elsevier.com/locate/aca

Optical immunosensor panel using quantum dot-antibody conjugates for highly sensitive detection of carbohydrate antigen 19–9 (CA19-9)

Daniela Oliveira [a], Pedro Oliveira [a], Ana Xu [a], Eduarda Rodrigues [a], Susana G. Guerreiro [b,c,d], Rafael C. Castro [e], David S.M. Ribeiro [e], João L.M. Santos [e], Ana Margarida L. Piloto [a,*]

[a] CIETI-LabRISE, School of Engineering, Polytechnic Institute, 4249-015, Porto, Portugal
[b] Institute for Research and Innovation in Health (i3S), 4200-135, Porto, Portugal
[c] Institute of Molecular Pathology and Immunology of the University of Porto - IPATIMUP, 4200-465, Porto, Portugal
[d] Department of Biomedicine, Biochemistry Unit, Faculty of Medicine, University of Porto, 4200-319, Porto, Portugal
[e] LAQV, REQUIMTE, Dept Chem Sci, Lab Appl Chem, Fac Pharm, University of Porto, 4050-453, Porto, Portugal

HIGHLIGHTS

- Quantum dot conjugates serve as optical sensors for CA19-9 antigen detection.
- A visual panel enables semi-quantitative tracking of CA19-9 levels in serum samples.
- This approach shows potential for detecting various cancer biomarkers in real samples.

GRAPHICAL ABSTRACT

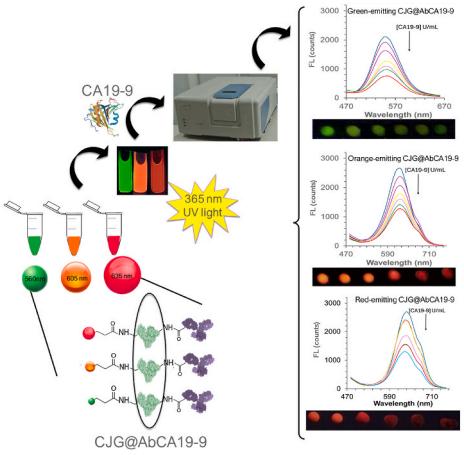

ARTICLE INFO

Handling Editor: Dr. J.P. Landers

Keywords:
Carbohydrate antigen 19–9 (CA19-9)
Pancreatic cancer (PC)
Quantum dots (QDs)
Fluorescent panel immunosensor

ABSTRACT

This study introduces a fluorescent immunosensor colour panel with antibody-conjugated quantum dots for detecting CA19-9 in human serum. The immunosensors presented decreasing fluorescence with increasing CA19-9 concentrations, with a linear detection range from 0.01 to 501.87 U mL^{-1} and detection limits of 1.66×10^{-4}, 2.71×10^{-4}, and 5.45×10^{-4} U mL^{-1} for the green-, orange-, and red-emitting conjugates in human serum. These limits are well below the 37 U mL^{-1} cutoff for early pancreatic cancer risk. The immunosensor panel is simple, sensitive, and specific, offering a visual colour readout for rapid CA19-9 detection, making it ideal for point-of-care applications. The results highlight the potential of the developed conjugates as a sensitive fluorescence colour panel for detecting CA19-9 across a wide range in human serum, both below and above the pancreatic

* Corresponding author.
E-mail addresses: amlpc@isep.ipp.pt, anamargaridapiloto@gmail.com (A.M.L. Piloto).

https://doi.org/10.1016/j.aca.2024.343399
Received 25 September 2024; Received in revised form 24 October 2024; Accepted 5 November 2024
Available online 7 November 2024

cancer cutoff. With just 200 μL of sample and a single pre-filtration step, the assay delivers results in under 15 min, offering a cost-effective and efficient platform for point-of-care use.

1. Introduction

The development of new sensors for diagnostic applications plays an important role in modern healthcare facilities. One of the key advantages is the ability to monitor diseases as cancer, not only at its early stages but also during its progression, which can lead to more successful treatment outcomes and improved patient survival rates. According to statistics from the Global Cancer Observatory, the five-year survival rate of pancreatic cancer (PC) patients is less than 8 %, nearly the lowest among existing cancers due to the lack of early and accurate diagnostic tools [1–3]. The cancer marker carbohydrate antigen 19–9 (CA19-9) is one of the most important tumour biomarkers in patients with gastrointestinal malignancies and it has a high prevalence in patients suffering from PC. Monitoring CA19-9 levels is therefore helpful in diagnosing PC and tracking its progression, providing healthcare professionals with a straightforward method for follow-up and in line with this, researchers have focused on developing point-of-care tests (PoCTs) for the quantification of CA19-9 biomarker [4–6].

In spite of ELISA representing a common approach for CA19-9 detection, it has drawbacks such as the high cost of the horseradish peroxidase (HRP) enzyme and environmental instability. Additionally, the substrate 3,3′,5,5′-tetramethylbenzidine (TMB) is sensitive to temperature and light. Therefore, a stable and inexpensive reporter that is less sensitive to oxidation processes holds potential for application as a new optical sensor system [7]. Semiconductor nanoparticles, known as quantum dots (QDs), have emerged as promising reporters due to their excellent characteristics, including broad absorption spectra, narrow, symmetrical, and size-tuneable emission spectra, as well as long photoluminescence lifetimes, good photostability, and high fluorescence quantum yields. QDs have a semiconductor core and a non-toxic shell, which make them thermally and photochemically stable. QDs, like other nanomaterials, exhibit unique properties due to their nanometer-scale dimensions, giving them characteristics that lie between those of bulk semiconductors and discrete molecules. Their optical and electronic properties change with both size and shape, making them attractive materials for developing sensor-based devices [8,9].

Proteins have been conjugated to the surface of QDs and several studies have utilized bovine serum albumin (BSA), enhancing their stability properties. BSA is chosen as the model protein due to its strong binding affinity to various nanoparticles, including QDs, gold nanoparticles, and silica nanoparticles, making it an ideal candidate for probe coatings [10,11]. Furthermore, the presence of amino and carboxylic acid residues in BSA molecules offsets advantageous reactive groups for establishing covalent linkages with the functional groups on the outer surface of probes [12,13]. In addition to BSA, antibodies are commonly employed in conjunction with various nanomaterials as targeting moieties for antigen recognition in the format of QDs@antibody-conjugates. However, the procedure for antibody conjugation to a fluorescent probe may lead to conformational changes in antibodies, potentially reducing their antigen-recognition ability [14,15]. Therefore, surface modification of QDs with target biomolecules, such as thiol groups, amino acids, and proteins, arises as an alternative route for conjugating appropriate ligands to the surface of QDs, providing them multifunctionality, selectivity, and sensitivity [16,17]. Additionally, carbonyldiimidazole (CDI) covalent conjugation methods take advantage of CDI as a highly reactive compound with an active carbonylating agent containing two acyl imidazole leaving groups. This crosslinker can react with a carboxylate ion to form an active N-acyl imidazole group capable of coupling with amine-containing molecules to form a stable covalent amide linkage [18,19].

In this study, a covalent method was employed to produce CdTe@MPA QDs coated with BSA and an antibody targeting the CA19-9 antigen. For this purpose, BSA was first covalently immobilized onto the surface of cadmium telluride QDs functionalized with mercaptopropionic acid CdTe@MPA QDs, through the activation of carboxylate ions in the presence of the CDI linker. The activated carboxylates of QDs were thus covalently bound to the amine groups on BSA, resulting in BSA-mediated QDs, denoted as BSA@QDs. Subsequently, the hydroxyl groups of CA19-9 antibodies (Ab CA19-9) were oxidized into reactive aldehydes and further reacted with the amine groups of the BSA-mediated QDs to form antibody-conjugates, designated as conjugates (CJG@AbCA19-9). The antigen targeting efficiency of the conjugates was evaluated as photoluminescent immunosensors for the quantification of CA19-9 in phosphate-buffered saline (PBS) 10 mM pH 7.4 and in commercial human serum. Finally, the synthesized conjugates were characterized using scanning electron microscopy (SEM), UV–vis spectroscopy, fluorescence spectroscopy, and Fourier transform infrared (FTIR) spectroscopy.

2. Experimental

2.1. Materials and reagents

Sodium periodate ($NaIO_4$, 99 %) was procured from VWR and 1,1′-carbonyldiimidazole (CDI, 99.0 %) was obtained from Merck. Absolute ethanol (>99 %) was sourced from Riedel-de Haën and 3-mercaptopropionic acid (MPA, 99 %) was acquired from TCI. Phosphate-buffered saline (PBS) and bovine serum albumin (BSA) were purchased from Amresco, purified mouse monoclonal CA19-9 antibody (Ab CA19-9), the human CA19-9 antigen grade protein unconjugated were obtained from abcam. Carcinoembryonic antigen (CEA) and matrix metalloproteinase 7 (MMP7) were purchased from abbexa, creatinine (CREA) and human serum albumin lyophilized powder (HSA) were purchased from Sigma. Commercial human serum at the normal range (HNS) was purchased from PZ CORMAY S.A., Poland, Amicon® ultracentrifuge filters (Ultra 0.5) MWCO 50 kDa were purchased from Sigma. All optical measurements were conducted using a QS High precision cell with a 1 mm light path made of quartz suprasil® from Hëllma® Analytics. All solutions were prepared using water from a Milli-Q system (specific conductivity <0.1 μS cm^{-1}), and employed chemicals of analytical grade quality. All reagents were used without further purification.

2.2. Apparatus

Scanning Electron Microscopy (SEM) images of the conjugates were take non a FEI Quanta 400 FEG, operating at an accelerating voltage of 15 kV. EDS images were also obtained. Transmission Electron Microscopy (TEM) images were taken on a JEOL JEM 1400 TEM at 120 kV (Tokyo, Japan) and digitally recorded using a CCD digital camera Orious 1100 W (Tokyo, Japan).

UV–vis spectra were obtained in the interval range (300–700 nm) on an Evolution 220 UV–vis spectrophotometer (Thermo Scientific). Measurements were performed with a Hellma suprasil quartz cell with a 1 mm optical path with solutions of the green-, orange- and red-emitting QDs at 1 μg mL^{-1} and with solutions of the correspondent conjugates at 1 μg mL^{-1} in PBS 10 mM pH 7.4.

FTIR spectroscopy was performed using a Nicolet iS100 spectrometer (Thermo Scientific) coupled to an attenuated total reflectance (ATR) sampling accessory of diamond contact crystal. Both sample and background spectra were acquired under the control of room temperature (r.t.) and humidity with 100 scans and a resolution of 16 cm^{-1} in the spectral range from 800 to 4000 cm^{-1}.

Fluorescence spectra were obtained on a Lumina fluorescence spectrometer (Thermo Scientific) equipped with a 150 W continuous wave xenon-arc discharge lamp as a light source at a scanning rate of 600 nm/min, a scan speed of 600 nm/min, an integration time of 50 ms and a response time of 0.02s. The photomultiplier tube voltage used was 300 PMT, both excitation and emission slits were set to 20 nm and both emission and excitation filters were set to air. Steady-state fluorescence mode was selected for the fluorescence measurements, using a Hellma suprasil quartz cell with a 1 mm optical path, with excitation at 410 nm and emissions recorded in the interval range between 470 nm and 770 nm, r. t. (22–23 °C). The fluorescence lifetimes were measured using a DeltaFlexTM TCSPC lifetime spectrofluorometer (Horiba Scientific, Kyoto, Japan).

2.3. Synthesis of the QDs nanoparticles

Aqueous soluble CdTe@MPA QDs were synthesized following a previously reported protocol with minor adjustments [20]. Initially, a three-neck flask containing 50 mL of ultrapure water, previously deaerated with nitrogen, was prepared. Cadmium chloride ($CdCl_2$, 1.23 g) was added to the flask, followed by the addition of 897 μL of mercaptopropionic acid (MPA) dissolved in 60 mL of ultrapure water. The pH of the solution was adjusted to 11.5 by the dropwise addition of 1 M sodium hydroxide. The resulting mixture was then heated to 80 °C under constant nitrogen flow. After, tellurium powder (0.384 g) was mixed with sodium borohydride (0.182 g) in 3 mL of deaerated ultrapure water, and the mixture was heated to 60 °C. The reaction mixture was refluxed at 120 °C for 30 min. By extending the refluxing time, the size of the quantum dots increased, and their colour shifted from green to red. Finally, the quantum dots were precipitated in ice-cold absolute ethanol (1:1) and centrifuged at 4000 rpm for 5 min. The resulting quantum dots were then dried in a desiccator protected from light, r. t. (Fig. 1 i).

2.4. Assembly of the immunosensor

The conjugates were synthesized using the following protocol. Briefly, green-, orange- and red-emitting CdTe@MPA QDs **1 (a–c)** (5.03 mg mL^{-1}) were activated with CDI linker (58.4 mg mL^{-1}) in ultrapure water at 60 °C for 20 min (Fig. 1 ii). Subsequently, BSA (10,4 mg mL^{-1}) was added to the CDI-mediated QDs, and the reaction mixture was stirred for 2 hs, r. t. (Fig. 1 iii). The mixture was centrifuged at 6000 rpm for 3 min, r. t. using ultracentrifuge filters with a 50 kDa cutoff to remove unconjugated products. The resulting BSA-mediated QDs, referred to as BSA@QDs **2 (a–c)** were stored protected from light for two weeks in PBS at 4 °C, as a stock solution (5.62 mg mL^{-1}).

The activation of the CA19-9 antibodies, followed a previously reported protocol to convert alcohols into reactive aldehydes [21]. Briefly, purified mouse monoclonal CA19-9 antibodies (Ab CA19-9) (30 μg mL^{-1}) were mixed with sodium periodate (21.4 mg mL^{-1}) in ultrapure water and reacted in the dark for 30 min r. t. (Fig. 1 iv). The activated antibodies were then suspended in 10 mM sodium carbonate at pH 9.8 and washed using ultracentrifuge filters with a 50 kDa cutoff to remove unreacted reagents. The activated antibodies were resuspended in 10 mM PBS pH 7.4 at a concentration of 10 μg mL^{-1} (**3**). Next the activated antibodies solution was reacted with BSA@QDs **2 (a–c)** (100 μg mL^{-1}) 4hs, r. t, resulting in the formation of the conjugates **4 (a–c)**. The conjugates were washed three times with PBS to remove unbound antibodies and resuspended in PBS 10 mM pH 7.4 yielding a stock solution of the green-, orange- and red-emitting conjugates at 60 μg mL^{-1}, 62 μg mL^{-1} and 63 μg mL^{-1}, respectively. These solutions were stored at 4 °C protected from light during 10 days. Solutions of the green-, orange- and red-emitting conjugates at 100 ng mL^{-1}, 500 ng mL^{-1} and 1 μg mL^{-1} in PBS 10 mM pH of 7.4 were prepared from the correspondent stock solutions and its fluorescence emission registered (Fig. S1). For more details, please see the ESM file, section S1.

2.5. Calibrations of the immunosensor

Solutions of the green- orange- and red-emitting conjugates were prepared using the following protocol. Briefly, 180 μL of a stock solution of conjugates in PBS 10 mM pH 7.4 were added to a 48-well microplate with 10 μL of standard solutions of CA19-9 prepared in the same buffer. The total volume was adjusted to 200 μL with PBS 10 mM pH 7.4, affording the conjugates at 100 ng mL^{-1} and the CA 19-9 standards in

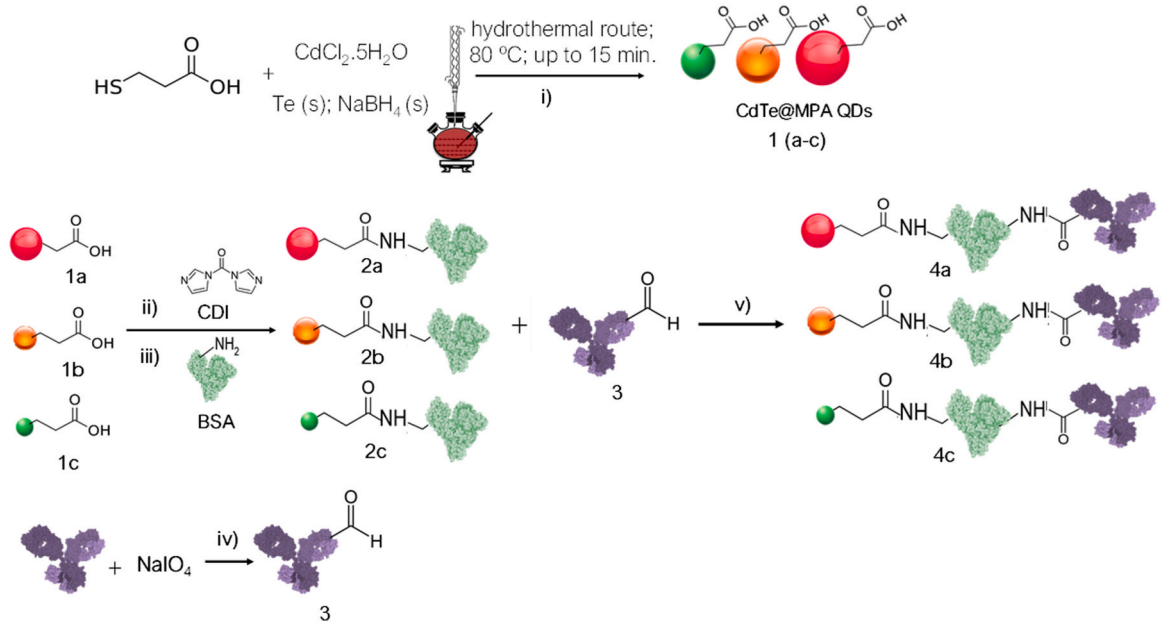

Fig. 1. Schematic representation of the synthesis of the conjugates **4 (a–c)**. Synthesis of the green-, orange- and red-emitting CdTe@MPA QDs **1 (a–c)** through the hydrothermal route (**i**); activation of the carboxylic groups of CdTe@MPA QDs with CDI (**ii**) and further reaction with free amines of BSA (**iii**) to obtain the conjugates BSA@QDs **2 (a–c)**; activation of the alcohol groups of the antibodies into reactive aldehydes with sodium periodate (**iv**) to obtain the activated antibodies **(3)**, finally conjugation of the activated antibodies **(3)** with BSA@QDs **2 (a–c)** to obtain the conjugates **4 (a–c)**. (For interpretation of the references to colour in this figure legend, the reader is referred to the Web version of this article.)

the interval range (0,01–501,9) U mL^{-1}. Replicates were prepared (S/N = 3) and incubated 15 min r. t. on a microplate shaker. After, the solutions were centrifuged and washed with bicarbonate buffer 10 mM to remove unbound probes and then the conjugates were resuspended in 200 μL PBS 10 mM pH 7.4. The fluorescence signal was measured as a function of the total CA19-9 concentration. The same protocol was applied to prepare the bioconjugates at 500 ng mL^{-1} and at 1 μg mL^{-1} in PBS 10 mM pH 7.4. In parallel, solutions of the raw QDs nanoparticles (1 μg mL^{-1}) in PBS 10 mM pH 7.4 were calibrated with standards of CA 19–9 prepared in the same interval range. The calibration protocols were repeated with the green-, orange- and red-emitting conjugates at 100 ng mL^{-1}, 500 ng mL^{-1} and 1 μg mL^{-1} and with the correspondent raw QDs nanoparticles (1 μg mL^{-1}) in lyophilized human serum within the normal range (HNS). This medium is used for routine quality control of inorganic, organic and enzymatic constituents. The human serum was previously filtered using ultracentrifuge filters (MWCO = 50 kDa) and used in the calibrations without further treatment. The fluorescence signal upon calibrations was measured as a function of the total CA19-9 concentration.

2.6. Reproducibility and stability of the immunosensor

The reproducibility of the immunosensors was evaluated by determining the amount of CA19-9 using the absolute calibration curves of each immunosensor spiked with standard solutions of CA19-9 at 5, 10, 100 and 500 U mL^{-1} in human serum. All assays were conducted in triplicate (S/N = 3) and the corresponding relative standard deviations calculated (RSD, %, n = 3).

The stability of the immunosensors was evaluated by storing replicates of green-, orange-, and red-emitting immunosensors in PBS 10 mM pH 7.4 at 4 °C, shielded from light, for 0, 5, 10, and 20 days. All assays were conducted in triplicate (S/N = 3) and the corresponding relative standard deviations calculated (RSD, %, n = 3).

2.7. Interference study

In the selectivity studies, the green-, orange- and red-emitting conjugates were tested using competition assays against four interferents, CEA, MMP7, CREA and HSA. Its selectivity was assessed for each interferent individually and in the presence of a fixed concentration of CA19-9. All assays were conducted in triplicate (S/N = 3) and the corresponding relative standard deviations calculated (RSD, %, n = 3).

3. Results and discussion

3.1. Assembly of the immunosensor

The surface mediation of quantum dots (QDs) using bovine serum albumin (BSA) molecules has been shown to enhance their stability and biocompatibility, particularly when the QDs are functionalized with carboxylic acid groups [21]. BSA serves as a stabilizing agent, providing a biocompatible coating around the QDs, which can prevent aggregation and reduce potential toxicity. In the conjugation process, 1,1′-carbonyldiimidazole (CDI) is initially used to activate the carboxylic acid groups present on the surface of the QDs (Fig. 1ii). CDI reacts with these groups to form a highly reactive intermediate known as N-acyl imidazole. This intermediate is generated due to the rapid release of carbon dioxide and imidazole, which drives the reaction forward. Subsequently, the activated carboxylate groups on the QDs interact with the amine groups present on BSA molecules, forming stable amide bonds. This conjugation process results in the formation of BSA-coated QDs (BSA@QDs), where the BSA molecules provide a protective layer around the QDs, enhancing their stability and biocompatibility (Fig. 1iii). To synthesize the conjugates, first sodium periodate was used as the oxidizing agent of the alcohol groups of N-glycans from CA19-9 antibodies, to be converted into reactive aldehydes (Fig. 1iv). Finally, the reactive aldehyde group-containing antibodies were conjugated to the amine groups of BSA@QDs to form the conjugates as CJG@AbCA19-9 (Fig. 1v). The fluorescence emission curves obtained during assembly of the green-, orange- and red-emitting conjugates in PBS 10 mM pH 7.4 are shown in Fig. S1 and compared with the correspondent raw QDs solutions. For more details please see ESM file, section S2.

3.2. SEM, EDS and TEM analysis

SEM images of the green-, orange- and red-emitting QDs conjugates can be seen in Fig. 2(a–c). All conjugates appear as aggregates with variable sizes up to 2 μm whose individual diameter is difficult to predict at the amplifications taken.

From the EDS analysis it is evidenced the presence of the elements cadmium and telluride, which are attributed to the metallic core of the nanoparticles and the presence of sulphur is associated to the mercaptopropionic acid used as the capping agent of the QDs. The elements carbon and oxygen are also detectable in all conjugates in significant amounts, probably related to the CA19-9 antibodies and the BSA protein molecules present at the surface of the conjugates Fig. 2 z1)-z3).

TEM images of the green-, orange- and red-emitting QDs conjugates can be seen in Fig. 2(*d*–f). All conjugates appear as aggregates with variable sizes up to 2 μm whose individual diameter is difficult to predict at the amplifications taken. The green-, orange and red-emitting QDs nanoparticles appear in TEM images as black spots representative of higher electron density materials, around shadowed structures evidenced as grey zones with lower image contrast and for this reason representative of the conjugates [22].

The conjugates were assembled around the BSA@QDs to which antibodies are covalently linked, forming BSA@QDs conjugates. All conjugates in solution appear aggregated, showing no significant size differentiation, with diameters up to 5 nm. These bulky structures appear as grey spots or shadowed areas in TEM images, characteristic of nonconductive materials, thus possessing reduced contrast around the core of the QDs [22].

3.3. UV–vis analysis

The green-, orange- and red-emitting QDs nanoparticles present an average size diameter around 2.5 nm, 2.9 nm and 3.7 nm respectively, determined according to a previous protocol [23]. The absorption spectra of the conjugate solutions followed the absorption profile of the raw QD nanoparticles in both intensity and wavelength range, with the conjugates absorbing within the same interval as the corresponding raw emitting QDs (Fig. 3A).

Both fluorescence emissions of solutions of the raw QDs nanoparticles and of the conjugates exhibit Gaussian-shaped functions, with the maximum emission wavelength increasing from the green-to the orange- and to the red-emitting conjugates from 550 nm to 600 nm–650 nm, respectively (Fig. 3B). The fluorescence emissions of all solutions of the conjugates evidence a decrease in its intensity comparatively to the solutions of the raw QDs nanoparticles prepared at the same concentration of 1 μg mL^{-1}, as shown in Fig. 3B which may be attributed to the conjugation of the BSA@QDs to CA19-9 antibodies.

3.4. FTIR analysis

In Fig. 4 is represented the FTIR measurements of the synthesized green (i), orange (ii) and red (iii) emitting CdTe@MPQA QDs, of the antibody CA19-9 (iv) and of the corresponding red-emitting conjugates (v).

In the FTIR spectra of the red-emitting QDs, the presence of the OH stretching is evidenced by the broad peak at 3329,23 cm^{-1} (Fig. 4A iii). The stretching modes of the C–H is seen at 2931,41 cm^{-1}. The typical thiol (S–H) weak vibrations appear at 2583,97 cm^{-1} at the QDs nanoparticles. The bands at 1552.08 cm^{-1} and 1392.71 cm^{-1} are attributed to

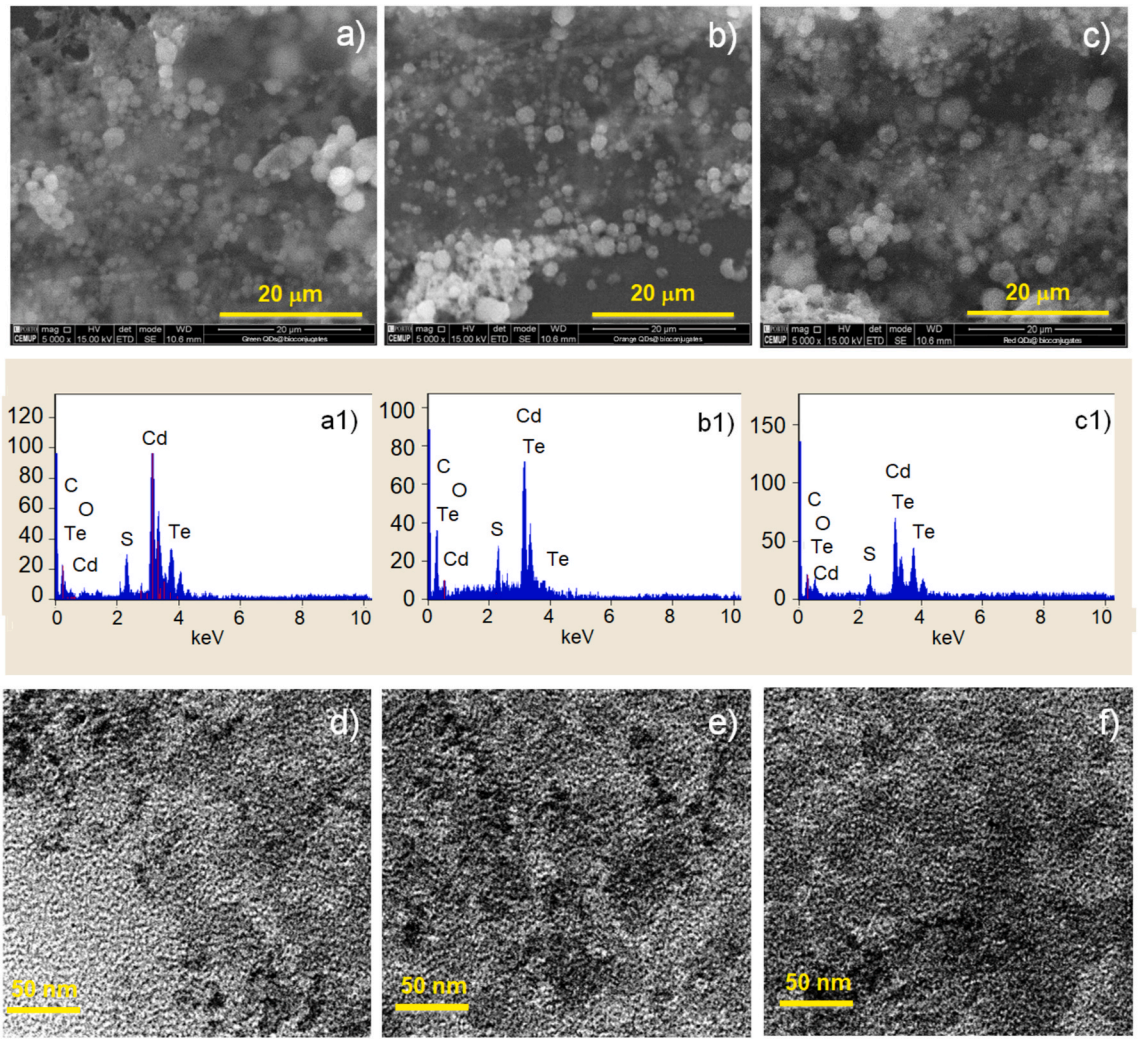

Fig. 2. SEM images of solutions of the green- (**a**), orange- (**b**) and red-emitting conjugates (**c**) and the correspondent EDS analysis **a1)**, **b1)** and **c1)**, respectively; TEM images of solutions of the green- (**d**), orange- (**e**) and red-emitting conjugates (**f**). (For interpretation of the references to colour in this figure legend, the reader is referred to the Web version of this article.)

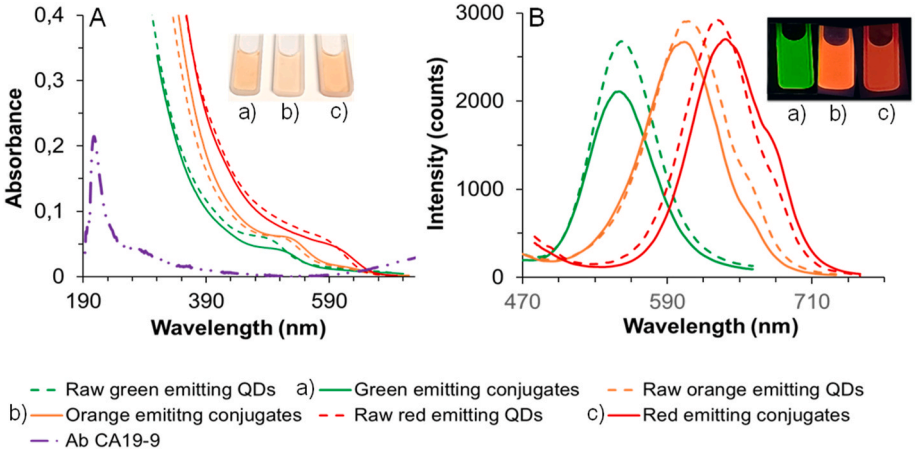

Fig. 3. (**A**) UV–Vis spectra of solutions of the green-, orange- and red-emitting CdTe@MPA QDs nanoparticles prepared at 1 µg mL^{-1} with distinct maximum absorption wavelengths. **a)** Green-emitting QDs (λ_{max} = 505 nm); **b)** orange-emitting QDs (λ_{max} = 525 nm) and **c)** red-emitting QDs (λ_{max} = 600 nm) in PBS 10 mM pH 7.4. Inset is the correspondent colour of each solution observed at ambient light. (**B**) The fluorescence emission spectra of the as prepared solutions. **a)** Green-emitting conjugates; **b)** orange-emitting conjugates **c)** red-emitting conjugates. Inset is the correspondent colour of each solution observed under a 365 nm UV lamp. (For interpretation of the references to colour in this figure legend, the reader is referred to the Web version of this article.)

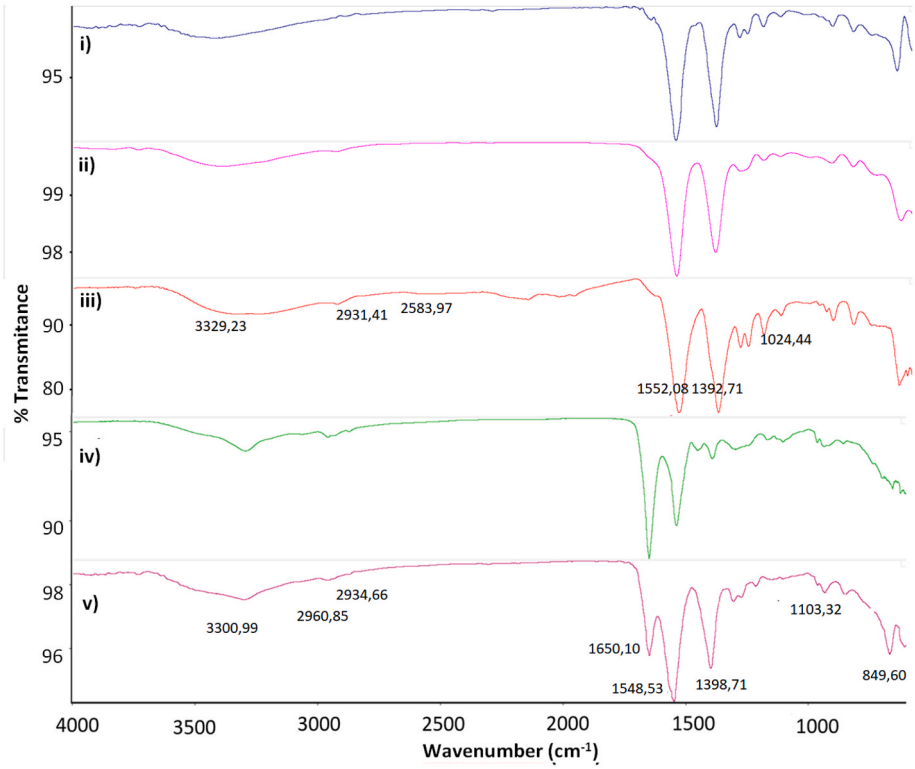

Fig. 4. FTIR spectra of the green- (**i**); orange- (**ii**) and red-emitting CdTe@MPA QDs (**iii**); of CA19-9 antibodies (iv) and of the corresponding red-emitting conjugates (v). (For interpretation of the references to colour in this figure legend, the reader is referred to the Web version of this article.)

the asymmetric and symmetric stretching vibrations of the carboxylate groups (COO^-) on the surface of the QDs nanoparticles. The strong peaks at these frequencies may be correlated with the fact that during the synthesis of all nanoparticles, the pH of the cadmium precursor solution was basic [24]. The band around 1024,44 cm^{-1} is attributed to the stretching vibrations of the C–*O*–C bonds. Besides, the bending vibration of C–S resulted in the absorption bands appearing at 849,60 cm^{-1} [25]. For simplicity of the FITR analysis, the spectra represented in Fig. 4B v is related to the red-emitting conjugates and the discussion provided is representative of the FTIR profile of all conjugates. The attenuated bands at 2960,85 cm^{-1} and 2934,66 cm^{-1} visible in the spectrum of the red-emitting conjugates (Fig. 4B v) and in the spectrum of the CA19-9 antibodies (Fig. 4B iv) are attributed to the N–H stretching vibrations from the amino acid residues of the antibodies. Moreover, the band at 1650,10 cm^{-1} seen on the spectrum of the red-emitting conjugates (Fig. 4B v) and of the spectrum of the CA19-9 antibodies (Fig. 4B iv) represent the N–H bending vibrations of the amino acid residues. The small band at 1103,32 cm^{-1} present in the red-emitting conjugates (Fig. 4B v) may be attributed to the amino acid residues from the C–N stretching of the antibodies, as some of these bands are also visible in its spectrum (Fig. 4B iv) [26]. The band appearing at 3300,99 cm^{-1} in the red-emitting conjugates (Fig. 4B v) is probably attributed to the OH stretching's of the QDs nanoparticles (Fig. 4A i - iii) as this band is present in all the three spectra of the nanoparticles. In addition, the bands at 1548,53 cm^{-1} and at 1398,71 cm^{-1} visible in the spectrum of the red-emitting conjugates (Fig. 4B v) and in all spectra of QDs nanoparticles (Fig. 4A i - iii) are attributed to the asymmetric and symmetric stretching's of the carboxylic groups of QDs, respectively [27].

3.5. Time-resolved fluorescence measurements

Time-resolved fluorescence measurements were conducted to assess the fluorescence lifetimes of green-, orange-, and red-emitting CdTe@MPA QDs and their corresponding bioconjugates with the CA19-9 antibody. The fluorescence decay profiles of both QDs and QD-antibody conjugates were modelled using three exponential decay components, which correspond to short, medium, and long-lived radiative processes, as shown in Fig. S4 and summarized in Table 1. This multi-exponential approach reflects the various emission pathways contributing to the overall fluorescence emission of the QDs. The average lifetime for each nanoparticle was then determined using equation (2):

$$\tau_{average} = \frac{\sum_i B_i \tau_i^2}{\sum_i B_i \tau_i} \quad (2)$$

wherein, B_i corresponds to the amplitude of each decay fraction and τ_i is the respective time constant.

The analysis of the average lifetimes of the raw QDs and of the bioconjugates upon functionalization with Ab CA19-9, provided important insights into the interaction between the QDs (sensing element) and the antibody (recognition element). It was observed that, despite the occurrence of fluorescence quenching, the lifetime of the QDs nanoparticles remained practically unchanged (Table 1 and Fig. S4) after binding to the antibodies. This result is significant because it suggests that the observed quenching is not due to alterations in the intrinsic properties of the QDs but rather due to a specific interaction process between the QDs and the antibodies. When QDs bind to antibodies, they form a stable complex. The preservation of the lifetime indicates that the radiative mechanisms responsible for the emission of the QDs were not affected by the antibody binding [28,29].

This finding is crucial for the design and application of QD-based biosensors, as it confirms that the interaction between the QDs and antibodies does not disturb the intrinsic photophysical properties of the QDs. The formation of the QD-antibody complex, evidenced by the fluorescence quenching and unchanged lifetime, supports the specificity and stability of the interaction, which is essential for accurate biosensing applications. For more details, please see ESM file, section S3.

Table 1
Fluorescence lifetime values of the raw green-, orange- and red-emitting QDs and of the correspondent QDs@conjugates, after functionalization with Ab CA19-9.

QDs entities	Fluorescence lifetimes	1st decay component	2nd decay component	3rd decay component	$\tau_{average}$ (ns)
Raw green QDs	τ_i (ns)	18.4 ± 0.5	3.6 ± 0.1	72 ± 0.8	58.1 ± 0.6
	B_i (%)	50.3	10.8	38.9	
Green QDs@conjugates	τ_I (ns)	9.3 ± 0.3	0.32 ± 0.02	58.9 ± 0.6	55.5 ± 0.5
	B_i (%)	24.7	19.7	55.6	
Raw orange QDs	τ_I (ns)	32 ± 1	5.5 ± 0.3	75 ± 1	57 ± 1
	B_i (%)	59.3	4.8	36.0	
Orange QDs@conjugates	τ_I (ns)	5.4 ± 0.6	33.6 ± 0.6	86 ± 1	61 ± 1
	B_i (%)	4.5	65.9	29.6	
Raw red QDs	τ_I (ns)	26.6 ± 0.7	5.0 ± 0.2	81 ± 1	62.5 ± 0.8
	B_i (%)	56.5	5.6	37.9	
Red QDs@conjugates	τ_I (ns)	20.2 ± 0.6	35.1 ± 0.6	0.05 ± 0.02	59.0 ± 0.6
	B_i (%)	26.4	51.7	22.0	

3.6. Fluorescence studies

The calibration curves for the conjugates and the corresponding raw QDs nanoparticles obtained with standard solutions of CA19-9 were analysed based on the Stern-Volmer equation (1).

$$I_0/I = 1 + k_{SV}\,[Q] \quad (1)$$

Here, I_0 and I are the fluorescence intensities in the absence and in the presence of CA19-9 respectively, k_{SV} is the Stern-Volmer constant, and [Q] is the total concentration of CA19-9 in solution [30].

3.6.1. Calibrations in PBS

A linear correlation in the fluorescence quenching (I_0/I) was observed at the maximum emission wavelength of each bioconjugate, in the interval range of [0,01–501,87] U mL^{-1}, as seen in Fig. 5, being its response more pronounced with the conjugates assembled at the concentration of 1 μg mL^{-1} of Ab CA19-9 (Fig. 5d–h, l, m, n, o). In Table S1 are shown the analytical results correspondent to the slopes calculated based on the Stern-Volmer equation. These results evidence that an increasing concentration of the Ab CA19-9 at the surface of the QDs nanoparticles up to 1 μg mL^{-1} is directly related with an increase of the interaction of the bioconjugate with the target antigen CA19-9, as evaluated but the slope values of the calibration curves obtained. For all conjugates, the limit of detection (LOD) was calculated as the concentration to quench three times the standard deviation of the blank divided by the slope. The green conjugates exhibited a LOD of 2,46 × 10^{-5} U mL^{-1} (S/N = 3) and a k_{SV} = −0,1091 (Table S1). In a similar way, the higher recognition ability of the immunosensors to CA19-9 target was observed with the orange-emitting conjugates (Fig. S2f) and the red-emitting conjugates prepared at the highest concentration of 1 μg mL^{-1} (Fig. S2i). In accordance to this, the orange conjugates exhibited a LOD of 2,40 × 10^{-4} U mL^{-1} (S/N = 3) and a k_{SV} = −0,1042, whereas the red-emitting conjugates exhibited a LOD of 4,41 × 10^{-4} U mL^{-1} (S/N = 3) and a k_{SV} = −0,1004 (Table S1).

From the calibration curves shown in Fig. 5, it is visible that the slope in the fluorescence signal associated to the quenching effect of the CA19-9 antigen is more pronounced for all conjugates prepared with 1 μg mL^{-1} of Ab CA19-9 (Fig. 5 m, n, o). This may be attributed to the presence of the Ab CA19-9 used in the assembly of the conjugates. According to Liu et al., as the raw QDs overlap in the UV–vis absorption region of Ab CA19-9 but not in the fluorescence emission region, is suggestive that the energy transfer could be excluded as one of the possible mechanisms for fluorescence quenching (Fig. 3A). Instead, a charge transfer phenomenon may be involved as the maximum absorption of Ab CA19-9 (200 nm) is in the same region as the absorption band of all colour-emitting QDs, enabling the charges in the conductive bands of QDs nanoparticles to transfer to the lowest unoccupied orbital of the Ab CA19-9 molecules. This occurrence may induce the extra fluorescence quenching observed during calibrations with increasing concentration of the Ab CA19-9 [31,32].

Finally, the calibrations with the raw QDs nanoparticles as controls of the correspondent conjugates also presented a signal decrease within the concentration range of the CA19-9 standard solutions in human serum, but at a lower extent (Fig. 5 m, n, o). Effectively, for the raw QDs nanoparticles the Stern-Volmer constant values obtained were lower and the LOD values appeared at higher limits compared to the corresponding conjugates assembled at any of the three concentrations (100 ng mL^{-1}, 500 ng mL^{-1} and 1 μg mL^{-1}) (Fig. S2, Table S1). For more details please see ESM file, section S2.

3.6.2. Calibrations in human serum

Upon resuspension of the conjugates prepared at 100 ng mL^{-1}, 500 ng mL^{-1} and at 1 μg mL^{-1} in the prefiltered non-diluted human serum (HNS), a fluorescence quenching up to 3 % of the initial signal was observed in the green-emitting conjugates, whereas a negligible decrease up to 0,4 % was observed with the orange- and the red-emitting conjugates, as shown in Fig. S1. This quenching effect may be attributed to the constituents naturally present in the human serum, which suppress the initial fluorescence signal of the QDs nanoparticles, being this variation more pronounced in the case of the conjugates prepared from the green-emitting QDs. This tendency is also observed for all raw QDs nanoparticles upon resuspension in human serum. Please see ESM file, section S2). Similarly to the calibrations conducted in PBS 10 mM pH 7.4, a linear correlation in the fluorescence quenching (I_0/I) was also observed at the maximum emission wavelength of each bioconjugate, in the interval range of [0,01–501,87] U mL^{-1} in human serum, being its response more pronounced with the conjugates assembled at the concentration of 1 μg mL^{-1} of Ab CA19-9 (Fig. 6d–**h**, **l**, **m**, **n**, **o)**. The analytical data correspondent to the calibration curves of the conjugates and the raw QDs nanoparticles in human serum is represented in Table S2 and was analysed according to the Stern-Volmer equation (1).

The green conjugates exhibited a LOD of 1,66 × 10^{-6} U mL^{-1} (S/N = 3) and a k_{SV} = −0,1241 (Table S2). In a similar way, the higher recognition ability of the immunosensors for CA19-9 was also observed with the orange-emitting conjugates (Fig. S3f) and the red-emitting conjugates prepared at the highest concentration of 1 μg mL^{-1} (Fig. S3i). In accordance to this, the orange conjugates exhibited a LOD of 2,71 × 10^{-4} U mL^{-1} (S/N = 3) and a k_{SV} = −0,1028, whereas the red-emitting conjugates exhibited a LOD of 5,45 × 10^{-4} U mL^{-1} (S/N = 3) and a k_{SV} = −0,1127 (Table S2). Finally, the calibrations with the raw QDs nanoparticles as controls of the correspondent conjugates also presented a signal decrease within the concentration range of the CA19-9 standards, but at a lower extent (Fig. 6 m, **n**, **o**). Indeed, its calibration curves presented lower Stern-Volmer constants and upper LOD values comparatively to the corresponding conjugates assembled at either concentrations of 100 ng mL^{-1}, 500 ngmL^{-1} or 1 μg mL^{-1} (Fig. S3, Table S2). For more details please see ESM file, section S2. It is evident that the calibrations in human serum were influenced by the presence of the normal levels of constituents of the serum, as there was an overall decrease in the sensing response of the conjugates and the raw QDs nanoparticles, comparatively to its response in PBS 10 mM pH 7.4.

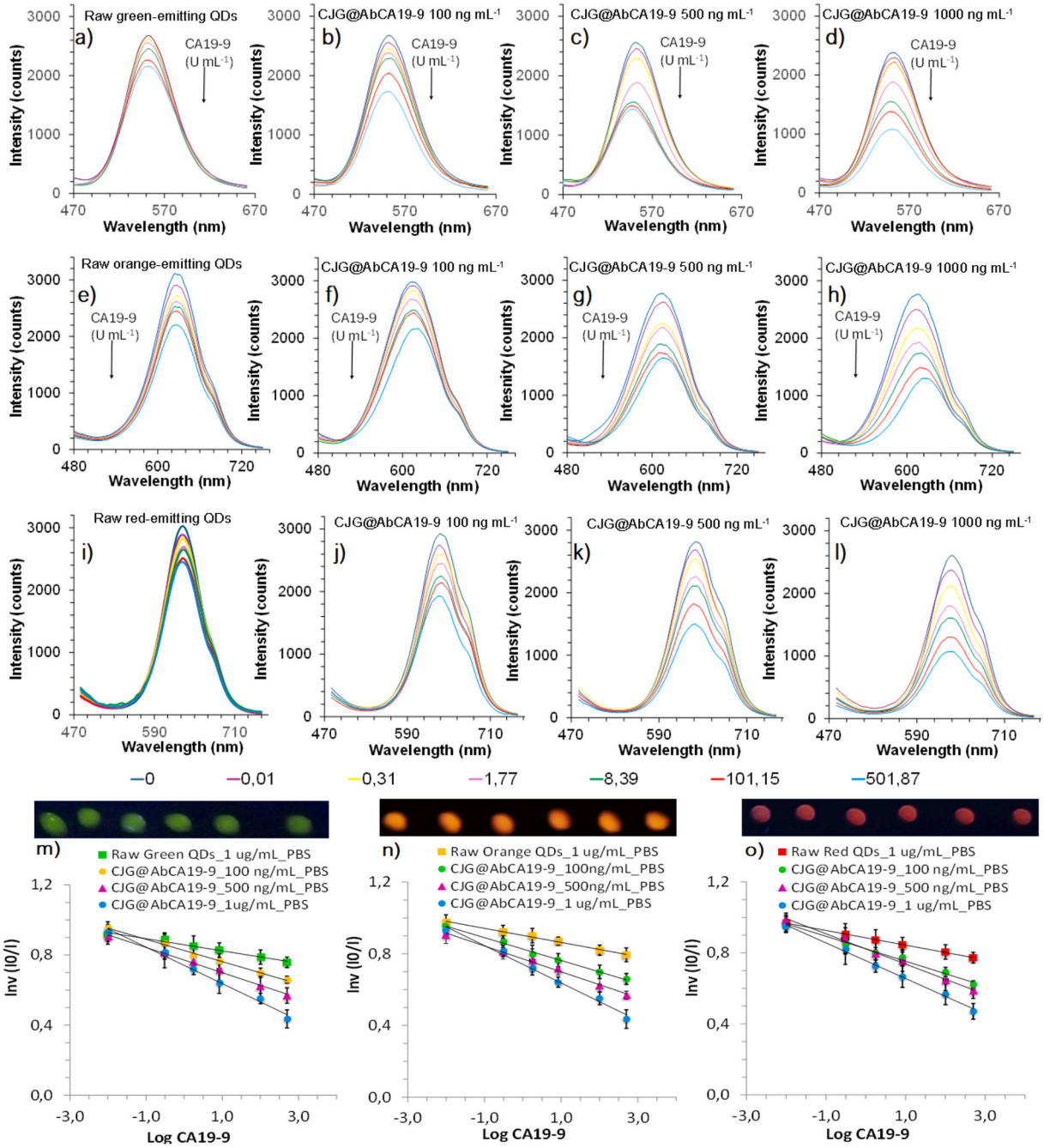

Fig. 5. Fluorescence emission spectra of the green- (**b-d**), orange- (**f-h**) and red-emitting-conjugates (**j-l**) at 100 ng mL^{-1}, 500 ng mL^{-1} and 1 μg mL^{-1} in PBS 10 mM pH 7.4, upon calibrations with CA19-9 standards in the interval range [0,01–501,87] U mL^{-1} and the correspondent Stern-Volmer plots (**m-o**). Fluorescence emission spectra of the green- (**a**), orange- (**e**) and red-emitting raw QDs (**i**) upon calibrations with the standards in the same interval range and the correspondent Stern-Volmer plots (**m-o**). (For interpretation of the references to colour in this figure legend, the reader is referred to the Web version of this article.)

Nonetheless, the results obtained from the LOD values and the interval of linearity obtained in serum demonstrate the ability of the conjugates to respond to the target analyte within the range of concentrations for CA19-9 for pancreatic cancer diagnosis. Moreover, the colour palette displayed by each immunosensor in human serum enables a multi-paneled colour match for the semi-qualitative quantification of CA19-9 levels. This approach provides more accurate quantification of target levels in a human serum sample by matching each immunosensor's colour with the corresponding colour palette from the CA19-9 standards. Finally, to ensure effective sensing, a platform must detect target biomarker levels above the cutoff value. In Table 2 are listed previously published CA19-9 sensors.

The immunosensors developed in this work demonstrated superior performance with lower LODs and broader linear ranges compared to other fluorescence- and electrochemical-based CA19-9 immunosensors. These improvements are critical, as they enhance the sensitivity and accuracy of detecting CA19-9. In clinical diagnostics, the dynamic range of an immunosensor is a key parameter. Pancreatic cancer patients often exhibit highly elevated levels of CA19-9, and the ability to accurately measure a wide range of concentrations is vital for effective monitoring of the disease. A broader linear range allows the immunosensor to detect both low and high concentrations of the biomarker, ensuring more reliable tracking of disease progression and treatment response. By offering both lower LOD and an extended dynamic range, these

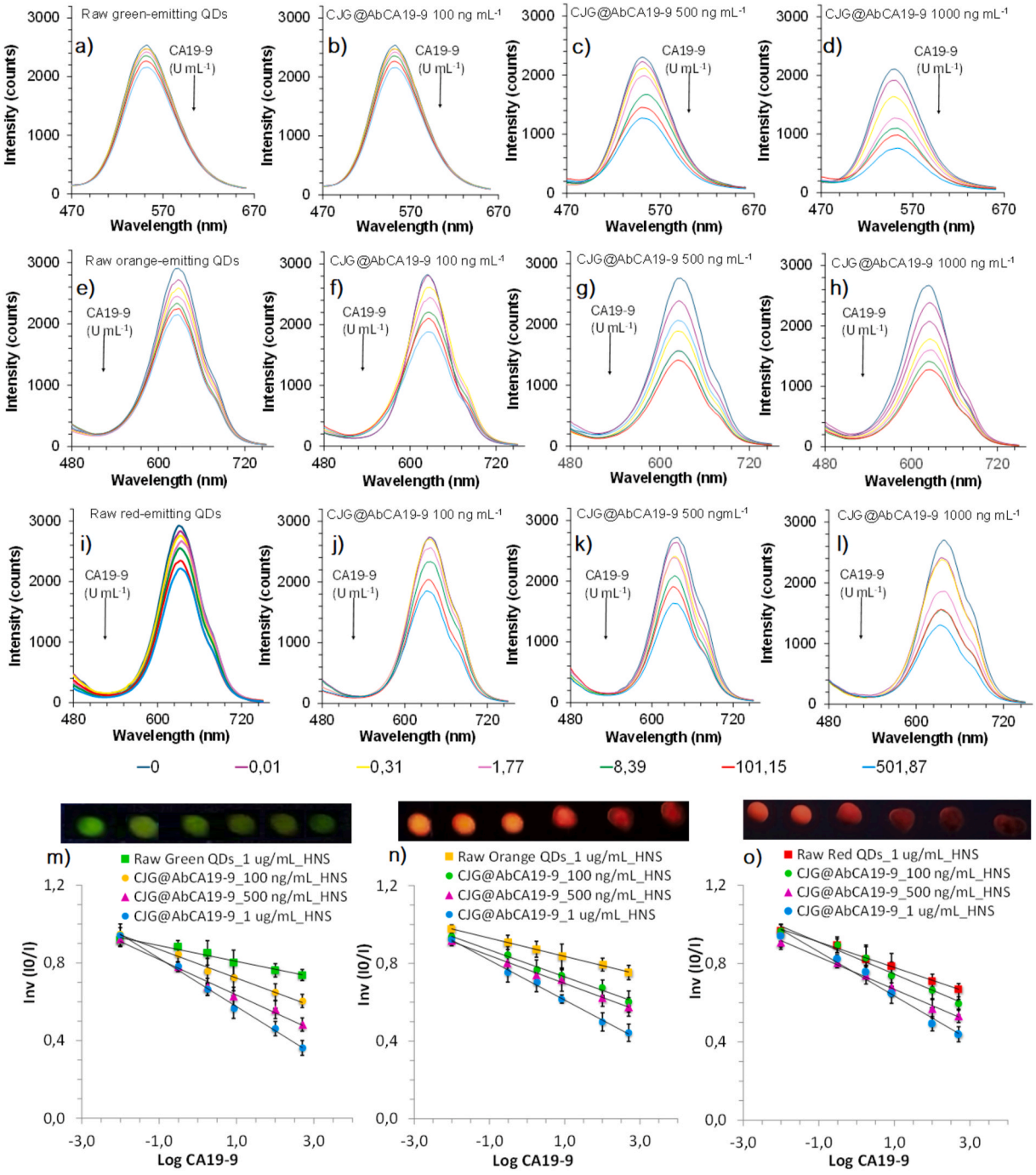

Fig. 6. Fluorescence emission spectra of the green- (**b-d**), orange (**f-h**) and red-emitting-conjugates (**j-l**) at 100, 500 and 1 μg mL^{-1} in human serum, upon calibrations with CA19-9 standards in the interval range [0,01–501,87] U mL^{-1} and the correspondent Stern-Volmer plots (**m-o**). Fluorescence emission spectra of the green- (**a**), orange- (**e**) and red-emitting raw QDs (**i**) upon calibrations with the standards in the same interval range and the correspondent Stern-Volmer plots (**m-o**). (For interpretation of the references to colour in this figure legend, the reader is referred to the Web version of this article.)

immunosensors provide enhanced clinical utility, potentially improving early diagnosis and enabling better patient management [43].

3.7. Reproducibility and stability of the immunosensor

The reproducibility of the immunosensors was evaluated calculating the average recovery using equation (3) and the results are shown in Fig. 7A and in Table 3.

$$\%\ recovery = \left(\frac{[CA19-9]\ spiked}{[CA19-9]found}\right) \times 100 \quad (3)$$

The results illustrate that the amounts of CA19-9 detected from the absolute calibration curves of each immunosensor align closely with the spiked samples, indicating no significant differences.

The stability of the immunosensors is shown in Fig. 7B. It is evidenced that storing the immunosensors for up to 10 days preserved its fluorescence signal at approximately 98 % of its initial intensity. However, extended storage led to a gradual decrease up to 95 % of its initial signal. This decline may be attributed to the potential toxicity of CdTe QDs, which could result in antibody denaturation and impact the viability of the immunosensors beyond the 10-day mark. For more details please see ESM file, section S4.

Table 2
Comparative responses of the green-, orange- and red-emitting immunosensors, CJG@AbCA19-9 developed in this work for detecting CA19-9 in human serum and comparison with other reported sensors.

Biosensor type	LRR (U mL^{-1})	LOD (U mL^{-1})	Ref.
Electrochemical	$1,5 \times 10^{-2}$ - $1,50 \times 10^{2}$	$6,0 \times 10^{-3}$	[33–37]
ECL	$1,0 \times 10^{-3}$ - $5,0 \times 10^{\circ}$	$5,0 \times 10^{-4}$	[38,39]
PEC	$5,0 \times 10^{-3}$ - $1,0 \times 10^{2}$	$1,1 \times 10^{-3}$	[40]
Quartz crystal microbalance	$1,55 \times 10^{1}$–$2,70 \times 10^{2}$	$8,3 \times 10^{\circ}$	[41]
Fluorescence	$1,0 \times 10^{-1}$ - $1,80 \times 10^{2}$	$4,0 \times 10^{-2}$	[42]
Fluorescence	$9,8 \times 10^{-3}$ - $5,0 \times 10^{2}$	$1,7 \times 10^{-4}$ green CJG@AbCA19-9 $2,7 \times 10^{-4}$ orange CJG@AbCA19-9 $5,4 \times 10^{-4}$ red CJG@AbCA19-9	This work

ECL: electrochemiluminescence; PEC: photoelectrochemical.

3.8. Interference study

The analytical response of the green-, orange- and red-emitting conjugates in the presence of the interferents CREA, MMP7, CEA and HSA was registered in human serum and compared to their fluorescence response in the presence of a standard solution of CA19-9 at 10 U mL^{-1}. The results are shown in Fig. 7C. In the presence of the target CA19-9, the fluorescence intensity of the green-, orange-, and red-emitting immunosensors decreased to 66 %, 64 % and 67 % of its initial intensity, respectively. It is observed that the fluorescence response of all

Table 3
Recoveries and relative standard deviations (RSD, %, n = 3) of the green-, orange- and red-emitting conjugates at 1 μg mL^{-1} upon spiking increasing concentrations of CA19-9 in human serum.

CJG@AbCA19-9	Sample	Spiked CA19-9 (U mL^{-1})	Found CA19-9 (U mL^{-1})	Recovery ± RSD (%)
Green-emitting	1	$5,00 \times 10^{\circ}$	$5,25 \times 10^{\circ}$	105,06 ± 1,11
	2	$1,00 \times 10^{1}$	$1,27 \times 10^{1}$	105,32 ± 1,47
	3	$1,00 \times 10^{2}$	$1,02 \times 10^{2}$	100,78 ± 0,63
	4	$5,00 \times 10^{2}$	$5,02 \times 10^{2}$	102,04 ± 1,30
Orange-emitting	1	$5,00 \times 10^{\circ}$	$5,17 \times 10^{\circ}$	103,34 ± 1,48
	2	$1,00 \times 10^{1}$	$1,07 \times 10^{1}$	101,45 ± 1,24
	3	$1,00 \times 10^{2}$	$1,07 \times 10^{2}$	103,47 ± 1,30
	4	$5,00 \times 10^{2}$	$5,01 \times 10^{2}$	101,09 ± 0,45
Red-emitting	1	$5,00 \times 10^{\circ}$	$5,21 \times 10^{\circ}$	104,19 ± 0,34
	2	$1,00 \times 10^{1}$	$1,06 \times 10^{1}$	101,15 ± 0,65
	3	$1,00 \times 10^{2}$	$1,05 \times 10^{2}$	102,28 ± 1,37
	4	$5,00 \times 10^{2}$	$5,04 \times 10^{2}$	104,11 ± 1,45

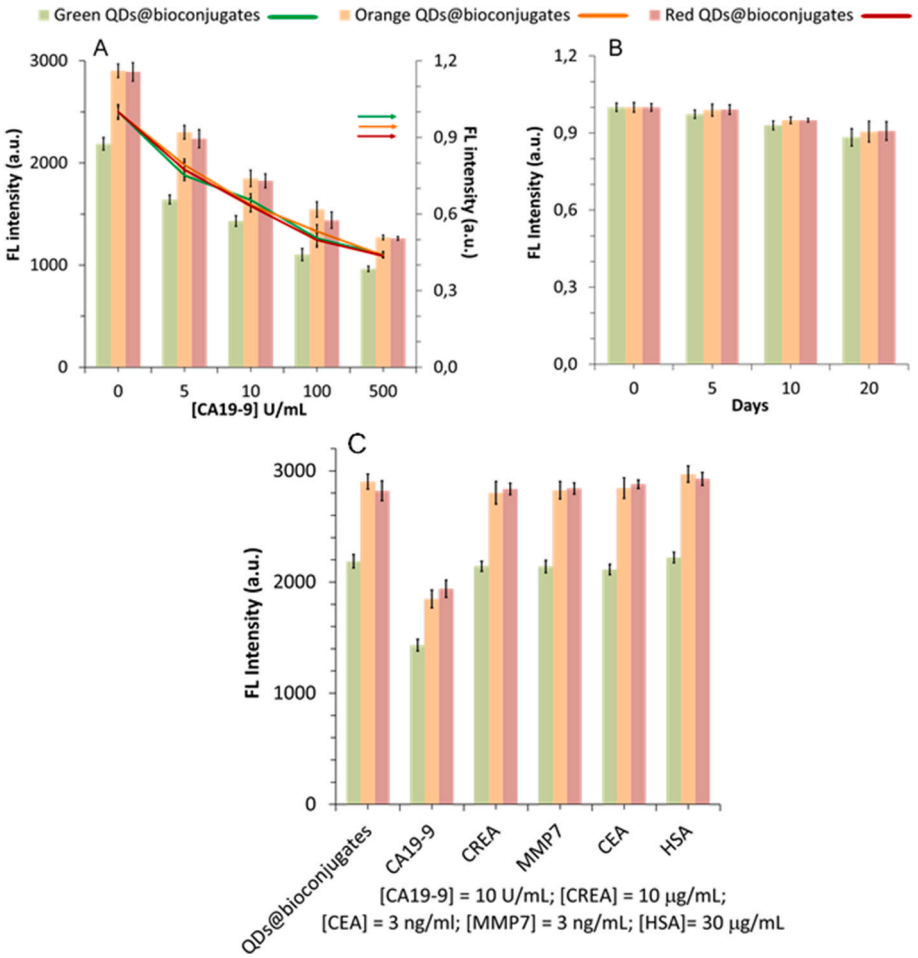

Fig. 7. (**A**) Evaluation of the reproducibility of the green-, orange- and red-emitting conjugates in determining the amount of CA19-9 using the absolute calibration curves of each immunosensor spiked with CA19-9 at 5, 10, 100 and 500 U mL^{-1} in human serum; (**B**) Stability of the green-, orange- and red-emitting conjugates prepared upon 20 days storage in PBS 10 mM pH 7.4; (**C**) Effect of four interferents in the fluorescence intensity of the green-, orange- and red-emitting conjugates in human serum (**C**) Error bars: SD, n = 3. (For interpretation of the references to colour in this figure legend, the reader is referred to the Web version of this article.)

conjugates in the presence of the interferents CREA, MMP7 and CEA decreased by 1,1 % up to 2,7 % of its initial signal.

The quenching effect caused by interferents CREA, CEA, and MMP7 may be attributed to its isoelectric points, regarding the acidic character of the human serum used (pH = 6.1) at 22 °C, which favours these biomolecules to have a positive surface charge in this medium [44]. Attending that the raw QDs are negatively charged due to the pKa of the mercaptopropionic acid, this leads to a fluorescence quenching effect from the three interferents in all bioconjugates [45]. Conversely, in the presence of HSA, the opposite effect is observed with an increase of the fluorescence signal of all conjugates up to 2,1 % to 2,9 % (RSD, %, n = 3). Given the isoelectric point of HSA, it is estimated to have a negative surface charge in the working buffer's pH. This enhances the emission signal of all bioconjugates in the presence of this protein [44]. For more details please see ESM file, section S5.

4. Conclusions

In the current study, three sensitive immunosensors were developed for CA19-9 antigen. The CdTe@MPA QDs nanoparticles used in this work were synthesized by the hydrothermal route, which confers them good fluorescence signal and reproducibility. The prepared immunosensors exhibited stable fluorescence emissions to allow for the quantification of CA19-9 in human serum and the LODs of all immunosensors reached values that enable for the quantification not only bellow the cutoff values associated to PC diagnosis but also above, as a means to monitor the disease's progression. In a visual three-colour panel code, the immunosensors provide a colour readout by matching each immunosensor's colour with the corresponding colour palette from the CA19-9 standards in human serum. This indicates that the conjugates developed in this work have potential for future research focused on developing fluorescence readout methods for other cancer biomarkers.

Funding

The authors acknowledge the Portuguese Foundation for Science and Technology (FCT, I.P.) for funding the project "Following up Cancer Biomarkers with New Biomimetic Optical Systems" (https://doi.org/10.54499/2022.07897.PTDC). Ana Margarida L. Piloto also thanks FCT, I.P., for her grant (SFRH/BPD/116067/2016), co-funded by the European Union's "Programa Operacional Regional Norte 2020," supported by the European Regional Development Fund (ERDF) and the European Social Fund (ESF). David S. M. Ribeiro acknowledges FCT, I.P., for funding through the DL 57/2016 program – Norma Transitória (DL 57/2016/CP1346/CT0033, DOI 10.54499/DL57/2016/CP1346/CT0033). Rafael C. Castro is grateful to FCT/MCTES and the ESF through NORTE 2020 for his PhD grant (ref. 2020.08465.BD, DOI 10.54499/2020.08465.BD). The authors further acknowledge partial support from FCT through grants UIDB/04730/2020 and UIDP/04730/2020.

CRediT authorship contribution statement

Daniela Oliveira: Visualization, Methodology, Investigation, Formal analysis. **Pedro Oliveira:** Investigation, Formal analysis. **Ana Xu:** Investigation, Formal analysis. **Eduarda Rodrigues:** Investigation, Formal analysis. **Susana G. Guerreiro:** Resources, Investigation, Formal analysis. **Rafael C. Castro:** Investigation, Formal analysis. **David S.M. Ribeiro:** Writing – review & editing, Validation, Supervision, Resources, Methodology, Investigation, Formal analysis. **João L.M. Santos:** Writing – review & editing, Visualization, Validation, Supervision, Resources, Methodology. **Ana Margarida L. Piloto:** Writing – review & editing, Visualization, Supervision, Project administration, Methodology, Funding acquisition, Conceptualization.

Declaration of competing interest

The authors declare that they have no known competing financial interests or personal relationships that could have appeared to influence the work reported in this paper.

Appendix A. Supplementary data

Supplementary data to this article can be found online at https://doi.org/10.1016/j.aca.2024.343399.

Data availability

Data will be made available on request.

References

[1] S. Mehrotra, P. Rai, A. Saxena, S. Priya, S.K. Sharma, Advancements in enzyme-based wearable sensors for health monitoring, Microchem. J. 200 (2024), https://doi.org/10.1016/j.microc.2024.110250.
[2] B. Kaur, S. Kumar, B.K. Kaushik, Novel wearable optical sensors for vital health monitoring systems—a review, Biosensors 13 (2023), https://doi.org/10.3390/bios13020181.
[3] R.L. Siegel, A.N. Giaquinto, A. Jemal, Cancer statistics, CA A Cancer J. Clin. 74 (2024), https://doi.org/10.3322/caac.21820, 2024.
[4] A.A. Patil, P. Kaushik, R.D. Jain, P.P. Dandekar, Assessment of urinary biomarkers for infectious diseases using lateral flow assays: a comprehensive overview, ACS Infect. Dis. 9 (2023), https://doi.org/10.1021/acsinfecdis.2c00449.
[5] S.S. Arya, S.B. Dias, H.F. Jelinek, L.J. Hadjileontiadis, A.M. Pappa, The convergence of traditional and digital biomarkers through AI-assisted biosensing: a new era in translational diagnostics? Biosens. Bioelectron. 235 (2023) https://doi.org/10.1016/j.bios.2023.115387.
[6] Z. Bradley, N. Bhalla, Point-of-care diagnostics for sepsis using clinical biomarkers and microfluidic technology, Biosens. Bioelectron. 227 (2023), https://doi.org/10.1016/j.bios.2023.115181.
[7] U. Laraib, S. Sargazi, A. Rahdar, M. Khatami, S. Pandey, Nanotechnology-based approaches for effective detection of tumor markers: a comprehensive state-of-the-art review, Int. J. Biol. Macromol. 195 (2022), https://doi.org/10.1016/j.ijbiomac.2021.12.052.
[8] S. Anilkumar Gandhi, P. Gopalbhai Sutariya, H. Nipulkumar Soni, D. Yashvantbhai Chaudhari, Quantum dots: application in medical science, Int. J. Nano Dimens. (IJND) 14 (2023), https://doi.org/10.22034/IJND.2022.1963190.2160.
[9] M.J. Molaei, Principles, mechanisms, and application of carbon quantum dots in sensors: a review, Anal. Methods 12 (2020), https://doi.org/10.1039/c9ay02696g.
[10] L.K. Boopathy, T. Gopal, A. Roy, R.R. Kalari Kandy, M.K. Arumugam, Recent trends in macromolecule-conjugated hybrid quantum dots for cancer theragnostic applications, RSC Adv. 13 (2023), https://doi.org/10.1039/d3ra02673f.
[11] J.Y. Lee, G. Soares, C. Doty, J. Park, J. Hovey, A. Schrader, H.S. Han, Versatile prepolymer platform for controlled tailoring of quantum dot surface properties, ACS Appl. Mater. Interfaces 16 (2024), https://doi.org/10.1021/acsami.4c00226.
[12] H. Zhang, G. Wang, Z. Zhang, J.H. Lei, T.M. Liu, G. Xing, C.X. Deng, Z. Tang, S. Qu, One step synthesis of efficient red emissive carbon dots and their bovine serum albumin composites with enhanced multi-photon fluorescence for in vivo bioimaging, Light Sci. Appl. 11 (2022), https://doi.org/10.1038/s41377-022-00798-5.
[13] D.J. Joshi, N.I. Malek, S.K. Kailasa, Fluorescence OFF-ON-OFF mechanism for the detection of digoxin, La3+, and epinephrine using bovine serum albumin functionalized molybdenum oxide quantum dots, Mater. Today Chem. 27 (2023), https://doi.org/10.1016/j.mtchem.2022.101291.
[14] A. Popov, V. Lisyte, A. Kausaite-Minkstimiene, E. Bernotiene, A. Ramanaviciene, Experimental evaluation of quantum dots and antibodies conjugation by surface plasmon resonance spectroscopy, Int. J. Mol. Sci. 23 (2022), https://doi.org/10.3390/ijms232012626.
[15] S. Centane, T. Nyokong, The antibody assisted detection of HER2 on a cobalt porphyrin binuclear framework and gold functionalized graphene quantum dots modified electrode, J. Electroanal. Chem. 880 (2021), https://doi.org/10.1016/j.jelechem.2020.114908.
[16] M. Deng, J. Li, B. Xiao, Z. Ren, Z. Li, H. Yu, J. Li, J. Wang, Z. Chen, X. Wang, Ultrasensitive label-free DNA detection based on solution-gated graphene transistors functionalized with carbon quantum dots, Anal. Chem. 94 (2022), https://doi.org/10.1021/acs.analchem.1c05309.
[17] H.S. Jung, K.J. Cho, Y. Seol, Y. Takagi, A. Dittmore, P.A. Roche, K.C. Neuman, Polydopamine encapsulation of fluorescent nanodiamonds for biomedical applications, Adv. Funct. Mater. 28 (2018), https://doi.org/10.1002/adfm.201801252.
[18] L. Wang, L. Xie, Z. Zhang, Determination of HER2 binding domain in antigen-antibody complexes based on chemical crosslinking mass spectrometry, J. Proteonomics 286 (2023), https://doi.org/10.1016/j.jprot.2023.104954.
[19] L.F. Hartje, D.A. Andales, L.P. Gintner, L.B. Johnson, Y.V. Li, C.D. Snow, Textile functionalization by porous protein crystal conjugation and guest molecule loading, Crystals 13 (2023), https://doi.org/10.3390/cryst13020352.

[20] A.M. Piloto, D.S.M. Ribeiro, S.S.M. Rodrigues, C. Santos, J.L.M. Santos, M.G. F. Sales, Plastic antibodies tailored on quantum dots for an optical detection of myoglobin down to the femtomolar range, Sci. Rep. 8 (2018), https://doi.org/10.1038/s41598-018-23271-z.
[21] S.L. Sahoo, C.H. Liu, M. Kumari, W.C. Wu, C.C. Wang, Biocompatible quantum dot-antibody conjugate for cell imaging, targeting and fluorometric immunoassay: crosslinking, characterization and applications, RSC Adv. 9 (2019), https://doi.org/10.1039/c9ra07352c.
[22] S. Utsunomiya, R.C. Ewing, Application of high-angle annular dark field scanning transmission electron microscopy, scanning transmission electron microscopy-energy dispersive X-ray spectrometry, and energy-filtered transmission electron microscopy to the characterization of nanopar, Environ. Sci. Technol. 37 (2003), https://doi.org/10.1021/es026053t.
[23] W.W. Yu, L. Qu, W. Guo, X. Peng, Experimental determination of the extinction coefficient of CdTe, CdSe and CdS nanocrystals, Chem. Mater. 16 (2004), https://doi.org/10.1021/cm033007z.
[24] A.M.L. Piloto, D.S.M. Ribeiro, S.S.M. Rodrigues, J.L.M. Santos, M.G. Ferreira Sales, Label-free quantum dot conjugates for human protein IL-2 based on molecularly imprinted polymers, Sensor. Actuator. B Chem. 304 (2020), https://doi.org/10.1016/j.snb.2019.127343.
[25] S. Premkumar, D. Nataraj, G. Bharathi, O.Y. Khyzhun, T.D. Thangadurai, Interfacial chemistry-modified QD-coupled CdTe solid nanowire and its hybrid with graphene quantum dots for enhanced photocurrent properties, ChemistrySelect 2 (2017), https://doi.org/10.1002/slct.201702352.
[26] P. Liu, Q. Wang, X. Zhou, X. Zhang, T. Fang, X. Min, X. Li, P. Leu, Thermodynamic and conformational investigation of the influence of CdTe QDs size on the toxic interaction with BSA, J. Photochem. Photobiol. Chem. 230 (2012), https://doi.org/10.1016/j.jphotochem.2011.12.014.
[27] M.S. Abd El-sadek, J. Ram Kumar, S. Moorthy Babu, The role of potassium tellurite as tellurium source in mercaptoacetic acid-capped CdTe nanoparticles, Curr. Appl. Phys. 10 (2010), https://doi.org/10.1016/j.cap.2009.06.016.
[28] R.C. Castro, R.N.M.J. Páscoa, M.L.M.F.S. Saraiva, J.L.M. Santos, D.S.M. Ribeiro, Photoluminescent and visual determination of ibandronic acid using a carbon dots/AgInS2 quantum dots ratiometric sensing platform, Spectrochim. Acta Mol. Biomol. Spectrosc. 267 (2022), https://doi.org/10.1016/j.saa.2021.120592.
[29] J.R. Lakowicz, Principles of Fluorescence Spectroscopy, Springer, 2006, https://doi.org/10.1007/978-0-387-46312-4.
[30] A. Virgilio, A.B.S. Silva, A.R.A. Nogueira, J.A. Nóbrega, G.L. Donati, Calculating limits of detection and defining working ranges for multi-signal calibration methods, J Anal At Spectrom 35 (2020), https://doi.org/10.1039/d0ja00212g.
[31] H. Liu, T. Ni, L. Mu, D. Zhang, J. Wang, S. Wang, B. Sun, Sensitive detection of pyrraline with a molecularly imprinted sensor based on metal-organic frameworks and quantum dots, Sensor. Actuator. B Chem. 256 (2018), https://doi.org/10.1016/j.snb.2017.10.048.
[32] J. Feng, Y. Tao, X. Shen, H. Jin, T. Zhou, Y. Zhou, L. Hu, D. Luo, S. Mei, Y.I. Lee, Highly sensitive and selective fluorescent sensor for tetrabromobisphenol-A in electronic waste samples using molecularly imprinted polymer coated quantum dots, Microchem. J. 144 (2019), https://doi.org/10.1016/j.microc.2018.08.041.
[33] F. Yang, Z. Yang, Y. Zhuo, Y. Chai, R. Yuan, Ultrasensitive electrochemical immunosensor for carbohydrate antigen 19-9 using Au/porous graphene nanocomposites as platform and Au@Pd core/shell bimetallic functionalized graphene nanocomposites as signal enhancers, Biosens. Bioelectron. 66 (2015), https://doi.org/10.1016/j.bios.2014.10.066.
[34] B. Li, Y. Li, C. Li, J. Yang, D. Liu, H. Wang, R. Xu, Y. Zhang, Q. Wei, An ultrasensitive split-type electrochemical immunosensor based on controlled-release strategy for detection of CA19-9, Biosens. Bioelectron. 227 (2023), https://doi.org/10.1016/j.bios.2023.115180.
[35] H. Rahmani, S.M. Majd, A. Salimi, Highly sensitive and selective detection of the pancreatic cancer biomarker CA 19-9 with the electrolyte-gated MoS2-based field-effect transistor immunosensor, Ionics 29 (2023), https://doi.org/10.1007/s11581-023-05136-2.
[36] H. Rahmani, S. Mansouri Majd, A. Salimi, F. Ghasemi, Ultrasensitive immunosensor for monitoring of CA 19-9 pancreatic cancer marker using electrolyte-gated TiS3 nanoribbons field-effect transistor, Talanta 257 (2023), https://doi.org/10.1016/j.talanta.2023.124336.
[37] F. Qi, M. Wu, S. Liu, W. Mu, C. Wu, X. Ren, C. Rui, F. Wu, D. Chang, H. Pan, Ratiometric electrochemical immunosensor for the detection of CA199 based on the ratios of NiCo@Fc-MWCNTs-LDH and 3D-rGOF@Ag/Au complexes, Talanta 272 (2024), https://doi.org/10.1016/j.talanta.2023.125606.
[38] D. Bahari, B. Babamiri, A. Salimi, R. Hallaj, S.M. Amininasab, A self-enhanced ECL-RET immunosensor for the detection of CA19-9 antigen based on Ru(bpy)2(phen-NH2)2+ - amine-rich nitrogen-doped carbon nanodots as probe and graphene oxide grafted hyperbranched aromatic polyamide as platform, Anal. Chim. Acta 1132 (2020), https://doi.org/10.1016/j.aca.2020.07.023.
[39] Y. Sha, Z. Guo, B. Chen, S. Wang, G. Ge, B. Qiu, X. Jiang, A one-step electrochemiluminescence immunosensor preparation for ultrasensitive detection of carbohydrate antigen 19-9 based on multi-functionalized graphene oxide, Biosens. Bioelectron. 66 (2015) 468–473, https://doi.org/10.1016/J.BIOS.2014.12.013.
[40] D. Gholamin, P. Karami, Y. Pahlavan, M. Johari-Ahar, Highly sensitive photoelectrochemical immunosensor for detecting cancer marker CA19-9 based on a new SnSe quantum dot, Microchim. Acta 190 (2023), https://doi.org/10.1007/s00604-023-05718-x.
[41] Y. Ding, J. Liu, X. Jin, H. Lu, G. Shen, R. Yu, Poly-L-lysine/hydroxyapatite/carbon nanotube hybrid nanocomposite applied for piezoelectric immunoassay of carbohydrate antigen 19-9, Analyst 133 (2008) 184–190, https://doi.org/10.1039/b713824e.
[42] B. Gu, C. Xu, C. Yang, S. Liu, M. Wang, ZnO quantum dot labelled immunosensor for carbohydrate antigen 19-9, Biosens. Bioelectron. 26 (2011) 2720–2723, https://doi.org/10.1016/J.BIOS.2010.09.031.
[43] Y. Kato, S. Takahashi, N. Gotohda, M. Konishi, Prognostic impact of the initial postoperative CA19-9 level in patients with extrahepatic bile duct cancer, J. Gastrointest. Surg. 20 (2016), https://doi.org/10.1007/s11605-016-3180-5.
[44] A.I. Frolov, S.V. Chankeshwara, Z. Abdulkarim, G.M. Ghiandoni, pIChemiSt — free tool for the calculation of isoelectric points of modified peptides, J. Chem. Inf. Model. 63 (2023), https://doi.org/10.1021/acs.jcim.2c01261.
[45] P. Paydary, P. Larese-Casanova, Water chemistry influences on long-term dissolution kinetics of CdSe/ZnS quantum dots, J. Environ. Sci. (China) 90 (2020), https://doi.org/10.1016/j.jes.2019.11.011.